

Supplementary information

S1 Comparison against another parcel model with condensation process

The details of the numerical model used in Ghan et al. (2011) can be found in Abdul-Razzak et al. (1998) describing the condensation process in an air parcel rising adiabatically at uniform speed. For comparison here, the DCPM is tested with a constant updraft velocity ($dV/dt = 0$, see Eq. 3 in Sect. 2.1) and both collision-coalescence and entrainment ($\mu = 0$) processes excluded. Hence, the condensation process determines activated particle numbers and corresponding maximum supersaturation in both numerical models. We also applied the same initial conditions and the same baseline case with a single lognormal aerosol distribution, as specified in Ghan et al. (2011). The number fraction activated is defined as the fraction of particles with wet sizes larger than their critical values (Nenes et al., 2001) when maximum supersaturation is achieved. Figs. S1–S6 demonstrate that the simulated maximum supersaturation and number fraction activated from the DCPM are in good agreement with the numerical solutions in Ghan et al. (2011) for a wide range of updraft velocities, aerosol number concentrations, geometric mean radii, geometric standard deviations, hygroscopicity, and condensation coefficients. As discussed in Sect. 4.2.1, collision-coalescence of cloud droplets is ineffective at early stages of the observed cloud due to small drop sizes developed and the condensation process dominates droplet growth in the 12 June case-study. Therefore, we can conclude that this comparison supports the validity of the present model and justify the findings from its application to the IPHEX case-study.

S2 Details of the IPHEX data

S2.1 Surface measurements

Figure S7 presents a general overview of the temporal variability in aerosol size distributions and total number concentrations from the SMPS and PCASP, respectively during the entire sampling period. To avoid episodic intrusion of long-range transport or local pollution, aerosol measurements with $N_{CN,SMPS} > 10,000 \text{ cm}^{-3}$ were removed from the analysis in order to isolate inherent properties of aerosol particles in the pristine forest environment of the SAM. The average total number concentration (\pm one standard deviation) of dry aerosol particles with diameters between 0.01 to 0.5 μm is $2,487 \pm 1,239 \text{ cm}^{-3}$, as sampled by the SMPS during the campaign (see Figs. S7a and b). Strong local fluctuations in number concentrations, in particular around midnight, are due to the presence of Aitken mode particles as indicated in Fig. S7a. These sharp increases in small particles are likely produced by the power engine in the Maggie Valley Sanitary District adjacent to the sampling site. The average total number concentration (\pm one standard deviation) of dry aerosol particles in accumulation and coarse modes (0.1–10 μm in diameter) is $1,106 \pm 427 \text{ cm}^{-3}$ as sampled by the PCASP during the campaign (see Figs. S7c and d). As expected, large particles from the PCASP show a much lower temporal variability in number concentrations as compared to small

particles from the SMPS. Similarly, their diurnal cycles (see Figs. S9a and b) exhibit relatively large temporal variations in $N_{CN,SMPS}$ while $N_{CN,PCASP}$ remain relatively stable throughout the day. Rainfall occurrences result in steep decreases in aerosol number concentrations, as shown in Figs. S7b and d.

As discussed before, κ and N_{CCN} were derived at six different supersaturation levels. In this study, we only show measurements collected at relatively high supersaturations (0.19–0.51%) as poor fits to D_{50} are often resulted due to low number concentration at $S = 0.09\%$ and 0.12% and thus no kappa value was reported. Figure S8 shows that both κ and N_{CCN} exhibit large temporal variabilities during the campaign. In Fig. S8a, the average value of κ (\pm one standard deviation) is 0.28 ± 0.09 at $S = 0.19\%$, 0.22 ± 0.08 at $S = 0.38\%$, 0.18 ± 0.07 at $S = 0.51\%$. In spite of local fluctuations in κ at each supersaturation level, larger κ values are generally obtained at lower supersaturation (Fig. S8a). A higher value of κ is derived from a larger D_{50} due to the fact that only large particles can be activated at a low supersaturation. Therefore, aerosol particles of different sizes are characterized with different hygroscopic properties. This is consistent with the finding from an earlier study in the Amazon rainforest showing that accumulation mode particles are more hygroscopic than Aiken mode particles (Gunthe et al., 2009). Note that the average κ values at each supersaturation level are comparable to subsaturated κ (0.14–0.46) measured in the southeastern United States (Nguyen et al., 2014) and the approximate global average ($\kappa \sim 0.3$) for continental aerosols (Andreae and Rosenfeld, 2008). At this surface site, the average N_{CCN} (\pm one standard deviation) is $569 \pm 208 \text{ cm}^{-3}$ at $S = 0.19\%$, $1,022 \pm 387 \text{ cm}^{-3}$ at $S = 0.38\%$, $1,210 \pm 505 \text{ cm}^{-3}$ at $S = 0.51\%$ (see Fig. S8b). The diurnal cycles in Fig. S9d indicate that N_{CCN} at $S = 0.19\%$ is remarkably stable while N_{CCN} at higher supersaturations (0.38% and 0.51%) exhibit pronounced variations throughout the day, likely linked to the changes in small particle concentrations (see Fig. S9a). In general, no evident diurnal cycles in κ and N_{CCN} are noted from the observations in Figs. S9c and d.

S2.2 Aircraft measurements

Coincidence errors have been identified in the CDP measurement, which cause droplet concentrations underestimation and droplet spectra broadening. Bulk LWC measurements from hot-wire probes can serve as independent observations to identify and correct coincidence-related sizing errors in the CDP. For example, during the flight on 12 June 2014, bulk LWC values from the King and Nevzorov probes are used to evaluate the CDP-derived LWC integrated from its droplet size distribution (see Eq. A7 in Appendix A). In this study, bulk LWC data with air temperature greater than 0°C and no particles above $50 \mu\text{m}$ (upper sizing threshold for the CDP) are considered in order to eliminate erroneous attribution of ice- or mix-phase particles to liquid water by hot-wire probes. In Fig. S11a, we can notice that CDP LWC produces a positive bias compared to LWC from the two hot-wire probes, whereas the King and Nevzorov probes demonstrate general agreement with each other. The CDP instrument aboard the UND Citation was modified by adding an optical mask, which has been proven to resolve the underestimation of droplet concentrations (Delene, 2016; Lance, 2012). Herein, we assume that the bias in CDP LWC is caused by the oversizing error rather than the undercounting error. Thus, we applied a correction to the CDP size distributions, as introduced by Painemal and Zuidema (2011). This bias can be removed based on the linear correlation revealed by the comparison between the King- and CDP-LWC using data collected during the first horizontal leg of the 12

June flight (see Fig. S11b). In the correction procedure, King LWC data between 0.05 and 0.6 g m⁻³ are taken into account. Thus, a linear regression with coefficient of determination $R^2 = 0.91$ is fitted between the CDP- and King-LWC and the derived slope (= 1.36 as denoted in Fig. S11b) is used to adjust CDP droplet size distributions. The modified droplet size in each bin is calculated by dividing the original size by $1.36^{1/3}$ (~ 1.1) to attain consistent LWC between the CDP and the King probe.

5 The corrected droplet size distributions slightly shift the measured spectra to smaller drop sizes (not shown here), thus providing confidence in the performance of the CDP probe during the campaign.

Fig. S15d displays the background aerosol concentrations measured by the CPC (lower cut-off diameter 10 nm) aboard the UND Citation along the complex terrain of the SAM (elevation along the flight transect is indicated by the black line) during the first horizontal leg (see flight track in Fig. 3a). Note aerosol concentrations sampled by the aircraft CPC
10 instrument are not corrected to standard temperature and pressure (STP). From east to west (flight direction as indicated by the blue arrow), it is noticeable that the three cloud regions (shaded in Fig. S15d) are linked to considerable drops in the aerosol concentrations. In particular, clouds form over the foothills of the ER (see location in Fig. 3a) in the inner region are associated with low-level moisture convergence from the east (Wilson and Barros, 2017). The cloud core sampled in this convergence zone is formed in intense updrafts (~ 8 m s⁻¹, see Fig. S15c) and it exhibits wide droplet spectra with heavier tails (larger drops)
15 than the observations in the IC core (updrafts ~ 1 – 2 m s⁻¹, see Fig. S15b). The in-cloud samples over high terrain elevations near the ECR (see location in Fig. 3a) also exhibit wide spectra but smaller number concentrations due to the formation of drizzle (Fig. S14d). As noted in Fig. S15d, significant increases ($\sim 1,000$ cm⁻³) in aerosol number concentrations are evident when the aircraft flew from the French Board (FB) valley into the inner SAM region that includes the Pisgah National Forest and the Great Smoky Mountains National Park (Figs. 1b and 3a). Generally, there is a close agreement between salient
20 topographic features and variations in aerosol number concentrations.

S3 Details of the WRF model configuration

A 5-day simulation (see the WRF domain configuration in Fig. 5a) over the SAM was performed using the advanced WRF model in version 3.5.1 (Skamarock et al., 2008) from 00:00 UTC 08 June for the first domain (06:00 UTC for second, third, and fourth domains) to 00:00 UTC 13 June 2014 for all four domains. The simulation was set up in a manner similar to
25 Wilson and Barros (2015) and Sun and Barros (2012). One-way nested domains are configured with horizontal grid spacing of 15-, 5-, 1.25-, 0.25-km. This corresponds to grid sizes of 147×121, 267×288, 552×552, and 555×555 for the first (D01), second (D02), third (D03), and fourth (D04) domains, respectively. A terrain-following vertical grid with 90 layers is constructed with 30 levels in the lowest 1 km AGL and the model top is at 50 hPa. Initialization and lateral boundary conditions are updated every 6-hour using the National Centers for Environmental Prediction (NCEP) Final Operational Global Analysis
30 (FNL) with 1°×1° horizontal resolution (Kalnay et al., 1996). The Kain-Fritsch cumulus parameterization scheme (Kain, 2004) is used in the D01 (15 km) and D02 (5 km) domains, and convection is resolved explicitly in the D03 (1.25 km) and D04 (0.25 km) domains. Other physics options include the Thompson cloud microphysics scheme (Thompson et al., 2008), a new version

of the Rapid Radiative Transfer Model radiation scheme for longwave and shortwave (Iacono et al., 2008), and the unified Noah land-surface model (Tewari et al., 2004) used for all four domains. The Mellor-Yamada-Janjic planetary boundary layer scheme (Janjic, 1994) is selected together with the Monin-Obukhov (Janjic Eta) surface layer scheme. The soil temperature and moisture fields are also initialized from the NCEP FNL data.

5 Analysis of model results along the trajectory of the first horizontal flight are shown in Figs S16, S17, and S18. Animations of horizontal and vertical wind fields at four distinct heights from the surface to the flight level can be viewed in Supplementary Animations SA1, SA2, SA3 and SA4. Figure S16 shows the instantaneous distribution of equivalent potential temperature (θ_e), and vertical and horizontal wind velocities from WRF simulations at 12:15 LT on 12 June 2014 along the trajectory of the first horizontal flight. Figure S17 shows the Lifting Condensation Level (LCL) and the Convective Boundary Layer (CBL) at the same time (12:15 LT). Figure S18 is the same as Fig. S16 at a different time-step (12:25 LT). The cloudy regions (blue shaded stripes) encountered in the flight are also marked, including the IC region. The vertical distribution of horizontal winds along the flight path is very heterogeneous and anisotropic due to the complex 3D structure of winds in the complex terrain of the inner region including shallow thermal upslope winds and ridge-valley circulations (e.g. Figs. S16c and S18c). At IC there is significant horizontal wind shear with westerly surface winds along the Pigeon valley and strong southerly mesoscale winds from roughly 1,500 m MSL and up. As noted in Figs. S16b and S18b, the magnitude of the measured instantaneous vertical velocity in the mid-valley region of IC do not exceed ± 1 m/s, whereas much higher instantaneous values up to 5m/s in the ER region at the mountain pass between the French-Broad and the Pigeon valleys are consistent with deeper cloud development inferred from the aircraft measurements. The CBL in the inner region is shallow and remains for the most part below the LCL (see Fig. S17). However, the release of mid-level instability, apparent from the folding of the isentropes in Figs. S16a and S18a showing an elevated layer of cold-air resulting from mesoscale southerly transport trapped between layers of warmer air, drives convective overturning (see arrows sketched at IC) and enhances vertical transport between the valley floor and the atmosphere above the ridges. This is similar to reports from previous mountain flow studies (e.g., De Wekker and Kossmann, 2015; Henne et al., 2004; Kossmann et al., 1999; Rotach et al., 2015; among others). The 3D wind fields are further illustrated by supplementary animations SA1, SA2, SA3, and SA4 of horizontal (blue vector) and vertical winds (colour contours) at four different elevation levels: near-surface (10 m AGL), ~1,500 m MSL, CBH level (~ 2,400 m MSL), and first horizontal leg level (~ 2,800 m MSL, flight track marked by the thick grey line). Note the time in the animations is in UTC and the conversion to LT is -4 hours. The red circle marks the IC region, the purple circle marks MV, and the black contours delineate the topography at an interval of 500 m. The animations show the patterns of southerly mesoscale horizontal transport above ridges, the complexity of the horizontal flow in the inner region underneath, and a mesoscale honeycomb like structure of weak to moderate updrafts and downdrafts with short-lived intensification (red colors) linked to overturning processes across the entire region. An exponential decay function is assumed for the vertical distribution of aerosol concentrations in the column to capture this vertical venting mechanism (Kossmann et al. 1999) consistent with the observed decrease of dry aerosol number concentrations with height between horizontal flight Leg 1 (~ 2,800 m MSL) and Leg 2 (~

3,700 m MSL) passing the same locations (not shown here). This is in keeping with previous cloud parcel (e.g., Eichel et al., 1996) and mesoscale modelling studies (Iguchi et al., 2008; Muhlbauer and Lohmann, 2008).

S4 Model simulations with surface aerosol concentrations at cloud base

As aerosol number concentrations and size distributions at and, or near cloud base were not sampled by the aircraft during IPHEX, they are extrapolated vertically from the surface aerosol number concentrations at MV by assuming an exponential decay with a scale height (H_s). This assumption is in keeping with the complex 3D structure of valley-ridge and mesoscales winds in the inner region of the SAM which makes it difficult to separate vertical and lateral venting processes from cross-ridge advection and remote transport as discussed in detail in Section 4.1. Considering ample field evidence of strong net vertical transport even when the Convective Boundary Layer (CBL) is shallow in mountain environments (e.g., Henne et al., 2004; Kossmann et al., 1999), we follow previous studies using mesoscale models (Iguchi et al., 2008; Muhlbauer and Lohmann, 2008) and cloud parcel models (e.g., Eichel et al., 1996). Nevertheless, for comparison additional simulations were conducted assuming relatively uniform vertical distribution of aerosol concentrations below cloud base, thus surface aerosol concentrations at MV (see Fig. 4 and Table 2) are used as initial aerosol input at cloud base for simulations at the IC region. Other assumptions and input parameters remain as specified in Sect. 4.1. Fig. S20 displays the sensitivity of simulated profiles of updraft velocity, supersaturation, total CDNC, and LWC to changes in a_c values ($[0.01, 1.0]$), as compared to the airborne observations (denoted by black crosses). As expected, reduced maximum supersaturation is obtained when high concentrations of surface aerosols are present (Fig. S20b). As noted in Fig. S20c, simulated CDNC with $a_c = 1$ achieves the best agreement with the airborne measurements, which is opposite to the findings of a small a_c value (0.01) in the reference simulations. The sensitivity of simulated droplet spectra at 1,600 m to variations in a_c from 0.01 to 1.0 are shown in Fig. S21, and the observed droplet spectrum, averaged from five individual CDP measurements between 1,500 m and 1,600 m, is indicated by the black dotted line. It is apparent that very narrow unrealistic droplet spectra are resulted from simulations with large values of a_c , in particular for $a_c = 1$ (see the red line). Although simulated CDNC with $a_c = 1$ is consistent with airborne measurements, the corresponding spectra prediction indicate large discrepancies with the observed spectra.

As demonstrated in Sect. 4.2.2, entrainment also have significant influence on the vertical structure of cloud drop concentrations. Again assuming surface aerosols at MV as initial aerosol concentrations at cloud base in IC and $a_c = 0.06$, variations in simulated profiles of updraft velocity, supersaturation, total CDNC, and LWC to changes in entrainment strength are illustrated in Fig. S22. By varying R from 200 m to 500 m, better agreement in vertical velocity, CDNC, and LWC is obtained between the simulation with strong entrainment strength ($R = 200$ m) and the observations (indicated by black crosses). When much higher a_c values are assumed (e.g., $a_c = 1$), even stronger entrainment is needed to attain consistent CDNC with the observations (not shown here). As shown in Fig. S23, the observed droplet spectrum (indicated by the black dotted line) is not well captured by the estimated droplet spectra at any altitude in the cloud. In summary, under the assumption of surface aerosol concentrations at cloud base (well mixed and deep convective boundary layer), good agreement in total

droplet numbers with the airborne observations can be achieved when large a_c or strong entrainment (small R) are assumed, however, the resulted droplet spectra in the predictions show large discrepancies with the observation.

References

- Abdul-Razzak, H., Ghan, S. J., and Rivera-Carpio, C.: A parameterization of aerosol activation: 1. Single aerosol type, *Journal of Geophysical Research: Atmospheres*, 103, 6123-6131, 10.1029/97jd03735, 1998.
- Andreae, M., and Rosenfeld, D.: Aerosol–cloud–precipitation interactions. Part 1. The nature and sources of cloud-active aerosols, *Earth-Science Reviews*, 89, 13-41, 2008.
- De Wekker, S. F. J., and Kossmann, M.: Convective Boundary Layer Heights Over Mountainous Terrain—A Review of Concepts, *Frontiers in Earth Science*, 3, 10.3389/feart.2015.00077, 2015.
- Delene, D. J.: Suitability of North Dakota for Conducting Effective Hygroscopic Seeding, *The Journal of Weather Modification*, 48, 43-67, 2016.
- Eichel, C., Krämer, M., Schütz, L., and Wurzler, S.: The water-soluble fraction of atmospheric aerosol particles and its influence on cloud microphysics, *Journal of Geophysical Research: Atmospheres*, 101, 29499-29510, 10.1029/96jd02245, 1996.
- Ghan, S. J., Abdul-Razzak, H., Nenes, A., Ming, Y., Liu, X., Ovchinnikov, M., Shipway, B., Meskhidze, N., Xu, J., and Shi, X.: Droplet nucleation: Physically-based parameterizations and comparative evaluation, *Journal of Advances in Modeling Earth Systems*, 3, 10.1029/2011ms000074, 2011.
- Gunthe, S. S., King, S. M., Rose, D., Chen, Q., Roldin, P., Farmer, D. K., Jimenez, J. L., Artaxo, P., Andreae, M. O., Martin, S. T., and Pöschl, U.: Cloud condensation nuclei in pristine tropical rainforest air of Amazonia: size-resolved measurements and modeling of atmospheric aerosol composition and CCN activity, *Atmospheric Chemistry and Physics*, 9, 7551-7575, 2009.
- Henne, S., Furger, M., Nyeki, S., Steinbacher, M., Neininger, B., De Wekker, S. F. J., Dommen, J., Spichtinger, N., Stohl, A., and Prevot, A. S. H.: Quantification of topographic venting of boundary layer air to the free troposphere, *Atmospheric Chemistry and Physics*, 4, 497-509, 2004.
- Iacono, M. J., Delamere, J. S., Mlawer, E. J., Shephard, M. W., Clough, S. A., and Collins, W. D.: Radiative forcing by long-lived greenhouse gases: Calculations with the AER radiative transfer models, *Journal of Geophysical Research*, 113, 10.1029/2008jd009944, 2008.
- Iguchi, T., Nakajima, T., Khain, A. P., Saito, K., Takemura, T., and Suzuki, K.: Modeling the influence of aerosols on cloud microphysical properties in the east Asia region using a mesoscale model coupled with a bin-based cloud microphysics scheme, *Journal of Geophysical Research*, 113, 10.1029/2007jd009774, 2008.
- Janjic, Z. I.: The step-mountain eta coordinate model: Further developments of the convection, viscous sublayer, and turbulence closure schemes, *Monthly Weather Review*, 122, 927-945, 1994.
- Kain, J. S.: The Kain–Fritsch convective parameterization: an update, *J. Appl. Meteorol.*, 43, 170–181, 2004.

- Kalnay, E., Kanamitsu, M., Kistler, R., Collins, W., Deaven, D., Gandin, L., Iredell, M., Saha, S., White, G., Woollen, J., Zhu, Y., Leetmaa, A., Reynolds, R., Chelliah, M., Ebisuzaki, W., Higgins, W., Janowiak, J., Mo, K. C., Ropelewski, C., Wang, J., Jenne, R., and Joseph, D.: The NCEP/NCAR 40-year reanalysis project, *Bull. Am. Meteorol. Soc.*, 77, 437–471, 1996.
- Kossmann, M., Corsmeier, U., De Wekker, S. F. J., Fiedler, F., Vögtlin, R., Kalthoff, N., Neininger, B., and Güsten, H.:
5 Observations of handover processes between the atmospheric boundary layer and the free troposphere over mountainous terrain, *Contributions to atmospheric physics*, 72, 329–350, 1999.
- Lance, S.: Coincidence Errors in a Cloud Droplet Probe (CDP) and a Cloud and Aerosol Spectrometer (CAS), and the Improved Performance of a Modified CDP, *Journal of Atmospheric and Oceanic Technology*, 29, 1532–1541, 10.1175/jtech-d-11-00208.1, 2012.
- 10 Muhlbauer, A., and Lohmann, U.: Sensitivity studies of the role of aerosols in warm-phase orographic precipitation in different dynamical flow regimes, *Journal of the Atmospheric Sciences*, 65, 2522–2542, 2008.
- Nenes, A., Ghan, S., Abdul-Razzak, H., Chuang, P. Y., and Seinfeld, J. H.: Kinetic limitations on cloud droplet formation and impact on cloud albedo, *Tellus B*, 53, 133–149, 2001.
- Nguyen, T. K. V., Petters, M. D., Suda, S. R., Guo, H., Weber, R. J., and Carlton, A. G.: Trends in particle-phase liquid water
15 during the Southern Oxidant and Aerosol Study, *Atmospheric Chemistry and Physics*, 14, 10911–10930, 10.5194/acp-14-10911-2014, 2014.
- Painemal, D., and Zuidema, P.: Assessment of MODIS cloud effective radius and optical thickness retrievals over the Southeast Pacific with VOCALS-REx in situ measurements, *Journal of Geophysical Research: Atmospheres*, 116, n/a–n/a, 10.1029/2011jd016155, 2011.
- 20 Rotach, M. W., Gohm, A., Lang, M. N., Leukauf, D., Stiperski, I., and Wagner, J. S.: On the Vertical Exchange of Heat, Mass, and Momentum Over Complex, Mountainous Terrain, *Frontiers in Earth Science*, 3, 10.3389/feart.2015.00076, 2015.
- Skamarock, W. C., Klemp, J. B., Dudhia, J., Gill, D. O., Barker, D. M., Wang, W., and Powers, J. G.: A description of the advanced research WRF version 3. Report TN-475+STR, National Center For Atmospheric Research, Boulder CO, 2008.
- Sun, X., and Barros, A. P.: The Impact of Forcing Datasets on the High-Resolution Simulation of Tropical Storm Ivan (2004)
25 in the Southern Appalachians, *Monthly Weather Review*, 140, 3300–3326, 10.1175/mwr-d-11-00345.1, 2012.
- Tewari, M., Chen, F., Wang, W., Dudhia, J., LeMone, M. A., Mitchell, K., Ek, M., Gayno, G., Wegiel, J., and Cuenca, R. H.: Implementation and verification of the unified NOAA land surface model in the WRF model, In 20th conference on weather analysis and forecasting/16th conference on numerical weather prediction, pp. 11–15, 2004.
- Thompson, G., Field, P. R., Rasmussen, R. M., and Hall, W. D.: Explicit Forecasts of Winter Precipitation Using an Improved Bulk Microphysics Scheme. Part II: Implementation of a New Snow Parameterization, *Monthly Weather Review*, 136, 5095–5115, 10.1175/2008mwr2387.1, 2008.
- 30 Wilson, A. M., and Barros, A. P.: Landform controls on low level moisture convergence and the diurnal cycle of warm season orographic rainfall in the Southern Appalachians, *Journal of Hydrology*, 531, 475–493, 10.1016/j.jhydrol.2015.10.068, 2015.
- Wilson, A. M., and Barros, A. P.: Orographic Land-Atmosphere Interactions and the Diurnal Cycle of Low Level Clouds and
35 Fog, *Journal of Hydrometeorology*, 10.1175/jhm-d-16-0186.1, 2017.

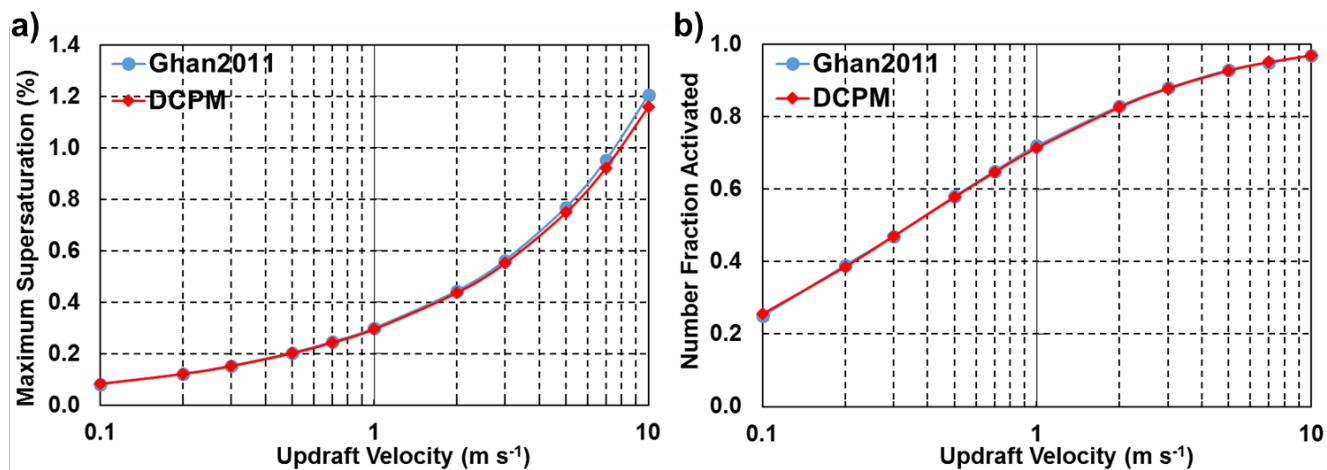


Figure S1: Maximum supersaturation (a) and number fraction activated as a function of updraft velocity calculated by the DCPM (red lines) compared to the numerical solution in Ghan et al., (2011; blue lines) using the same initial conditions and aerosol properties. In the baseline case, the aerosols have number concentration of 1000 cm^{-3} , geometric mean radius of $0.05 \text{ }\mu\text{m}$, a geometric standard deviation of 2, and a hygroscopicity of 0.7; the condensation coefficient is 1.0 and the uniform updraft is 0.5 m s^{-1} .

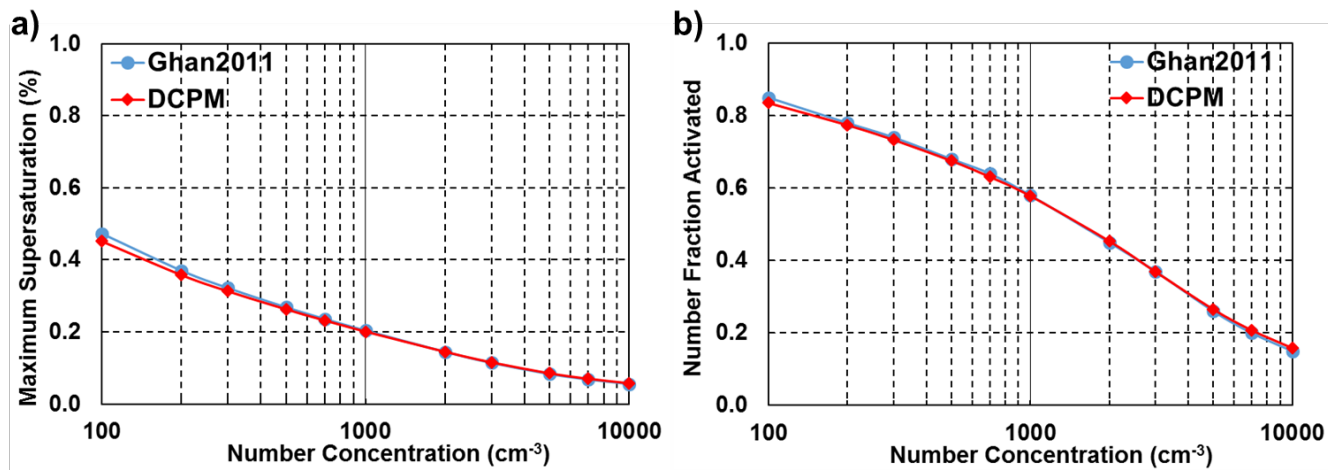


Figure S2: As in Fig. S1 but as a function of aerosol number concentration.

5

10

15

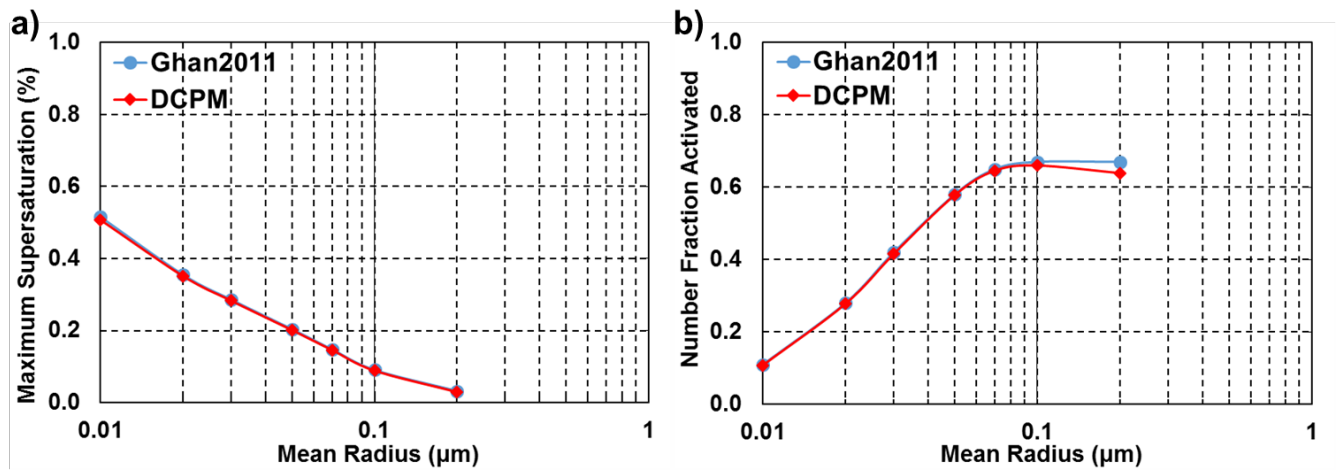


Figure S3: As in Fig. S1 but as a function of geometric mean radius of the single lognormal aerosol distribution.

5

10

15

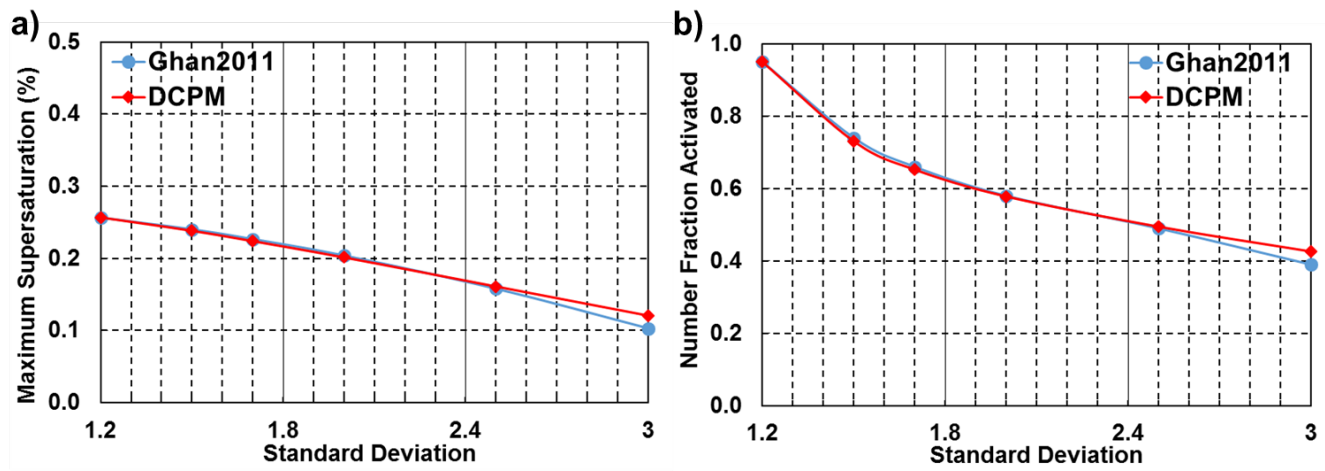


Figure S4: As in Fig. S1 but as a function of geometric standard deviation of the single lognormal aerosol distribution.

5

10

15

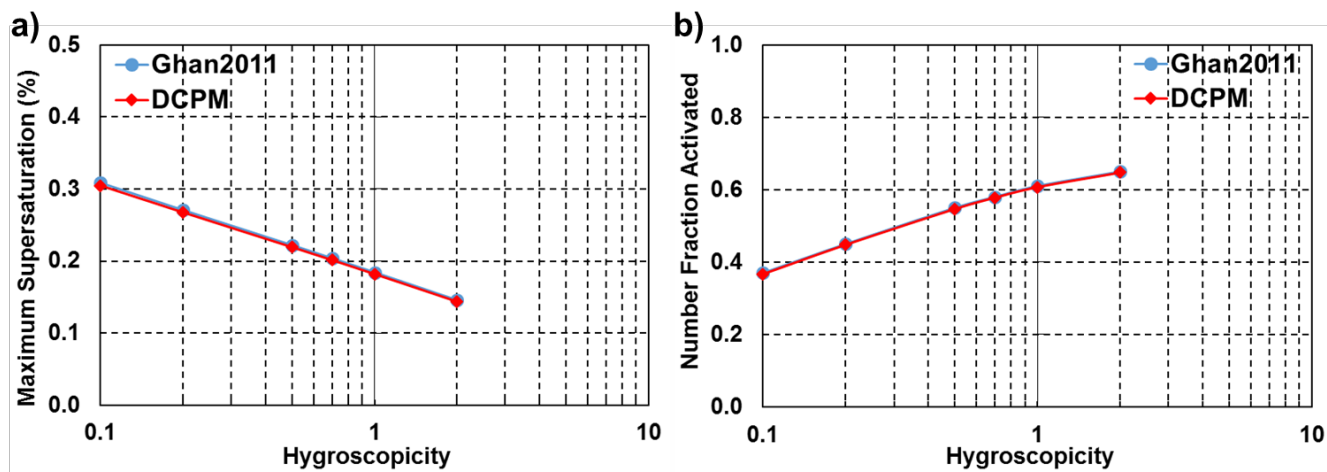


Figure S5: As in Fig. S1 but as a function of hygroscopicity.

5

10

15

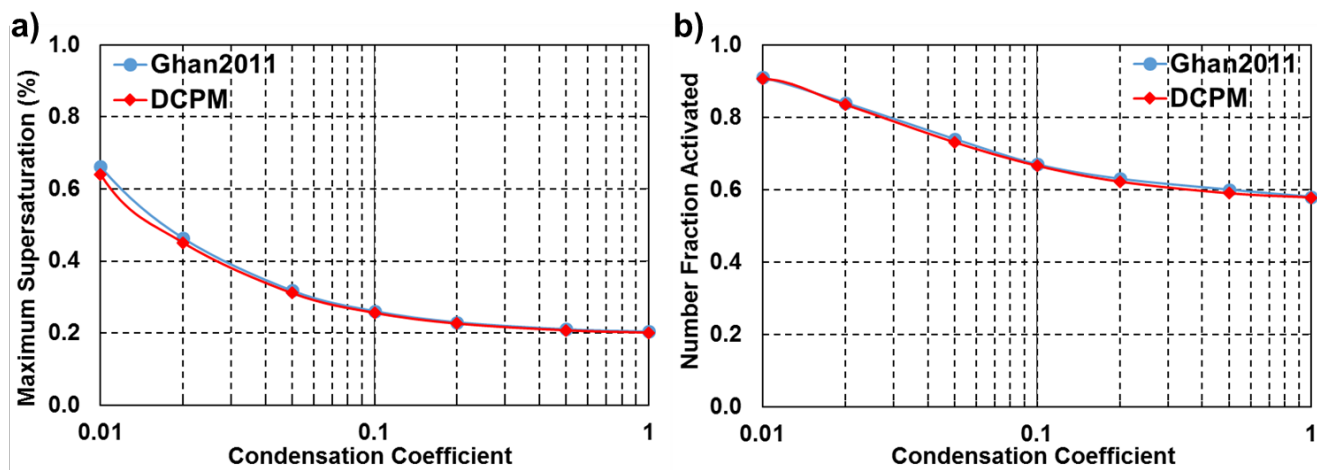


Figure S6: As in Fig. S1 but as a function of condensation coefficient.

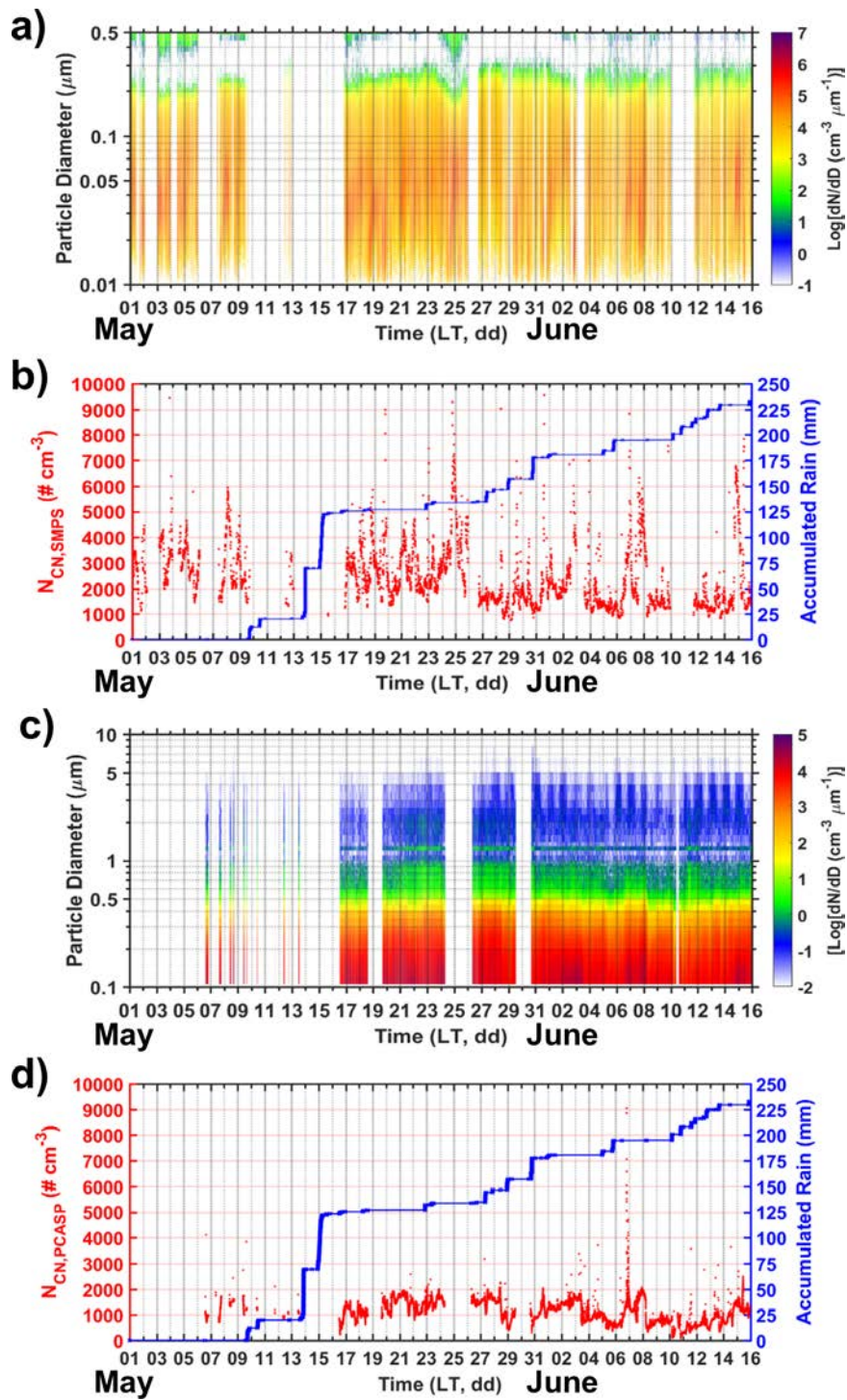


Figure S7: Time series of dry aerosol size distribution and total number concentration (N_{CN}) from the SMPS (a, b) and PCASP (c, d), respectively, measured at MV during the IPHEX IOP. Discontinuities in the data are associated with delayed installation (PCASP), rainfall occurrences, and occasional instrument malfunction.

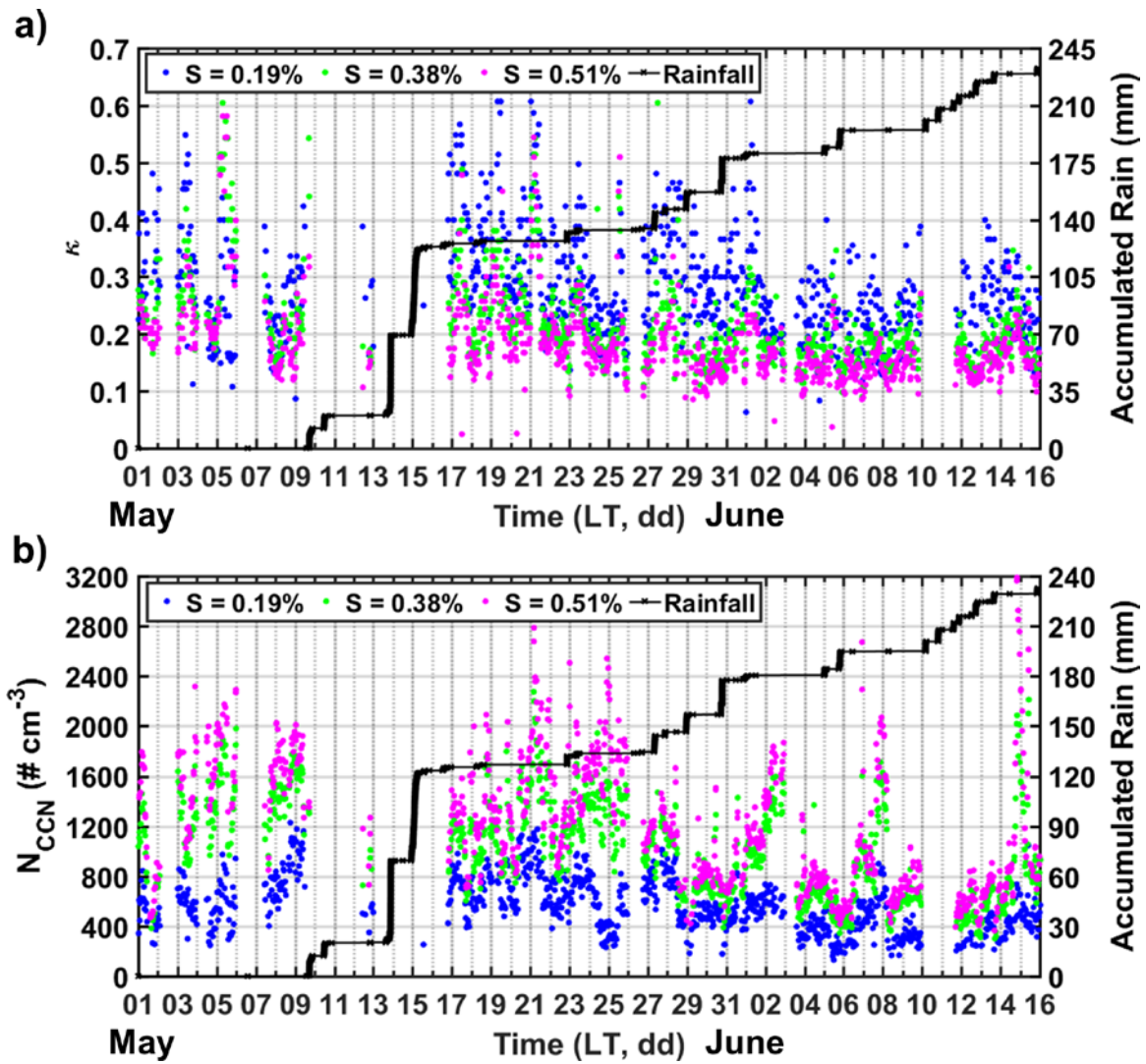


Figure S8: Time series of hygroscopicity parameter (κ , a) and CCN concentration (N_{CCN} , b) at three supersaturation levels, measured at MV during the IPHEX IOP. Discontinuities in the data are associated with rainfall occurrences and occasional instrument malfunction.

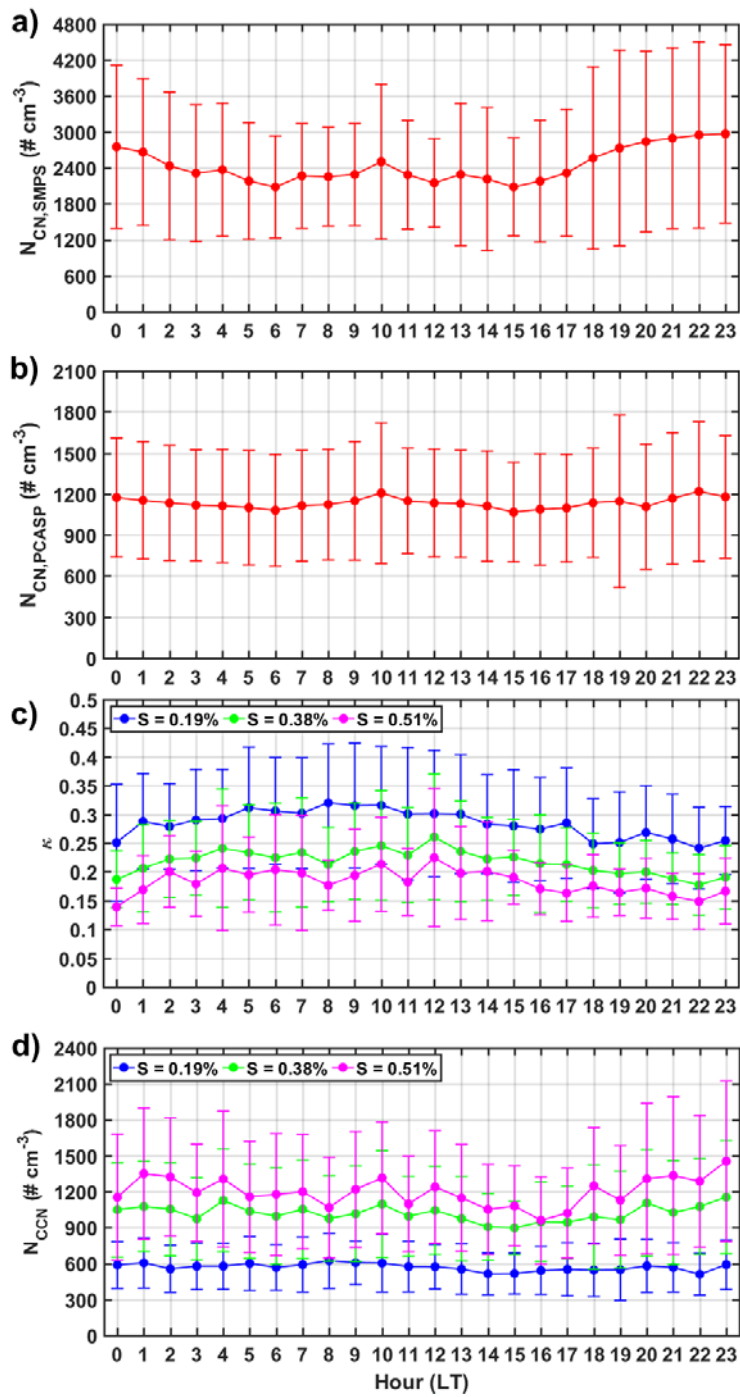


Figure S9: Diurnal cycles in total aerosol number concentrations from the SMPS ($N_{CN,SMPS}$, a) and PCASP ($N_{CN,PCASP}$, b), and in hygroscopicity parameter (κ , c) and CCN concentration (N_{CCN} , d) at three supersaturation (S) levels measured at MV during the IPHEX IOP. Mean values are denoted as solid circles and sample variability is indicated by short vertical bars, representing plus and minus one standard deviation.

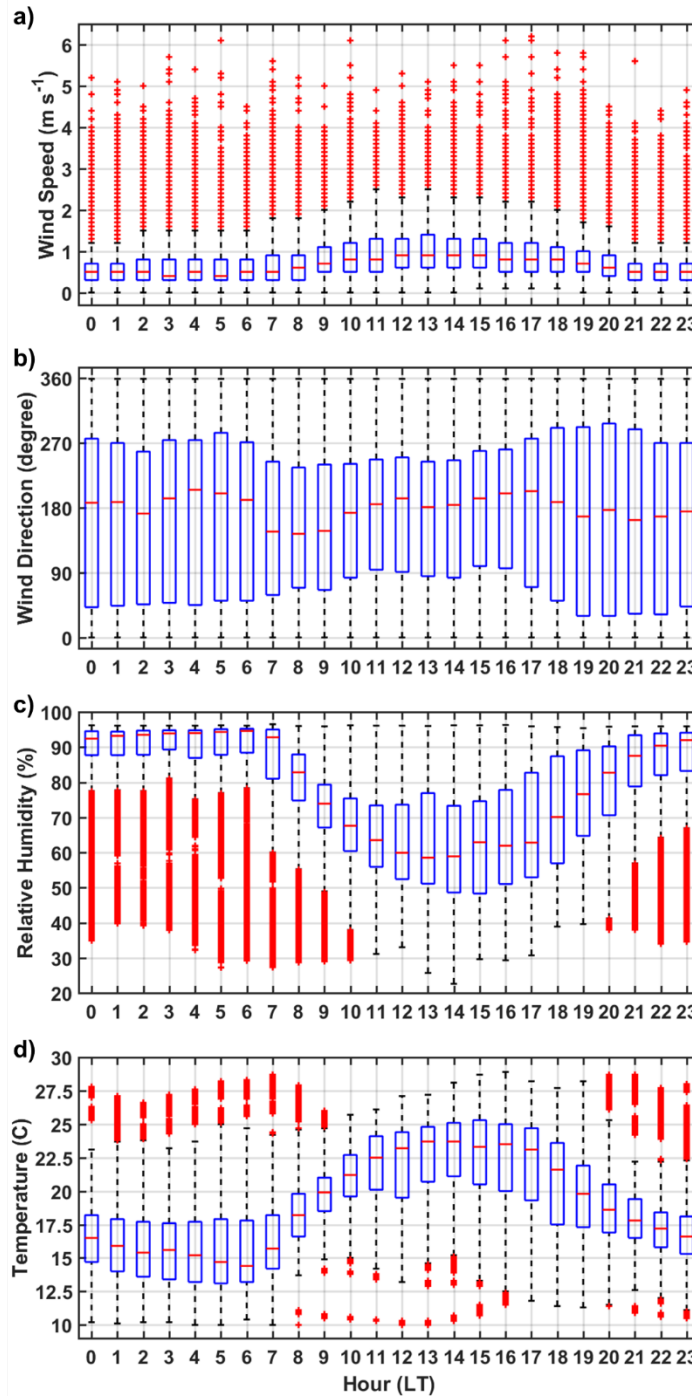


Figure S10: Diurnal cycles in local meteorological variables: wind speed (a), wind direction (b), relative humidity (c), and ambient temperature (d), measured at MV during the IPHEX IOP. The blue box represents the interquartile range (IQR) from the lower quartile (25th) to the upper quartile (75th), and the red short horizontal line inside the box indicates the median. The two horizontal black lines (“whiskers”) extending from the central box denote the ± 1.5 IQR interval, and red plus signs mark outliers that fall out of ± 1.5 IQR.

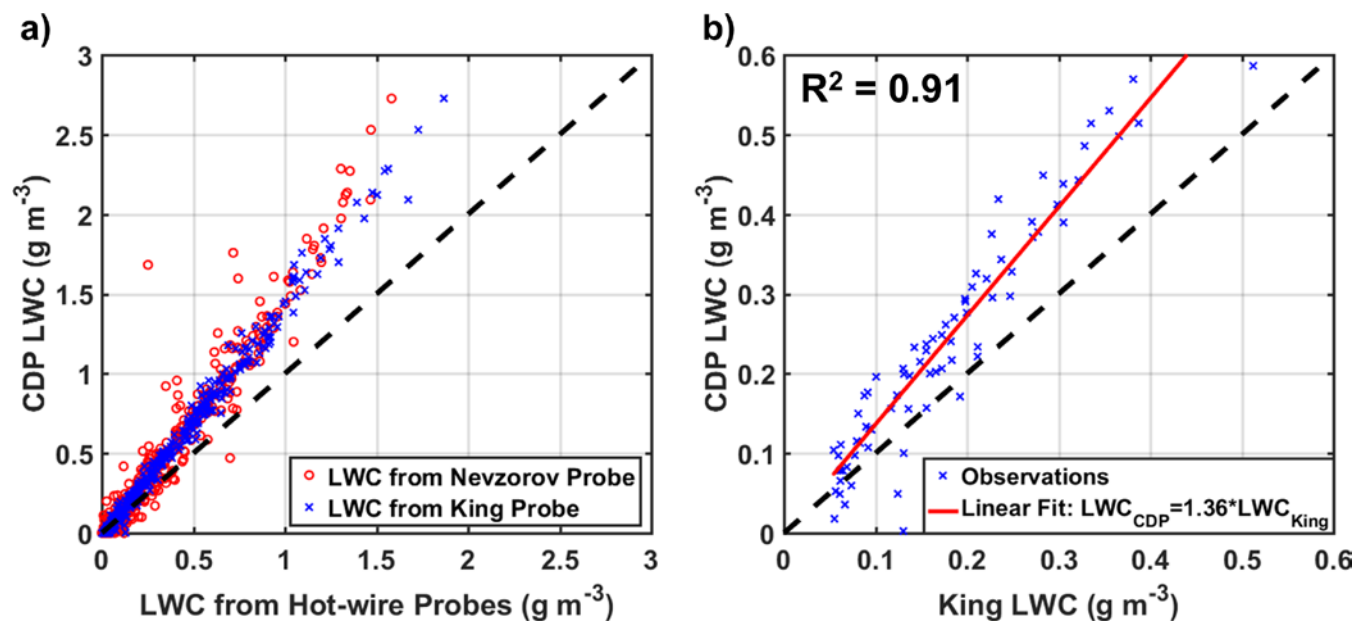


Figure S11: a) Scatterplot for LWC from the CDP and two hot-wire probes (the King and Nevzorov probes), sampled during the 12 June flight. b) LWC observations from the CDP and the King probe during the first horizontal cloud transect on the same day are fitted by a linear regression (represented by the red line) with coefficient of determination $R^2 = 0.91$.

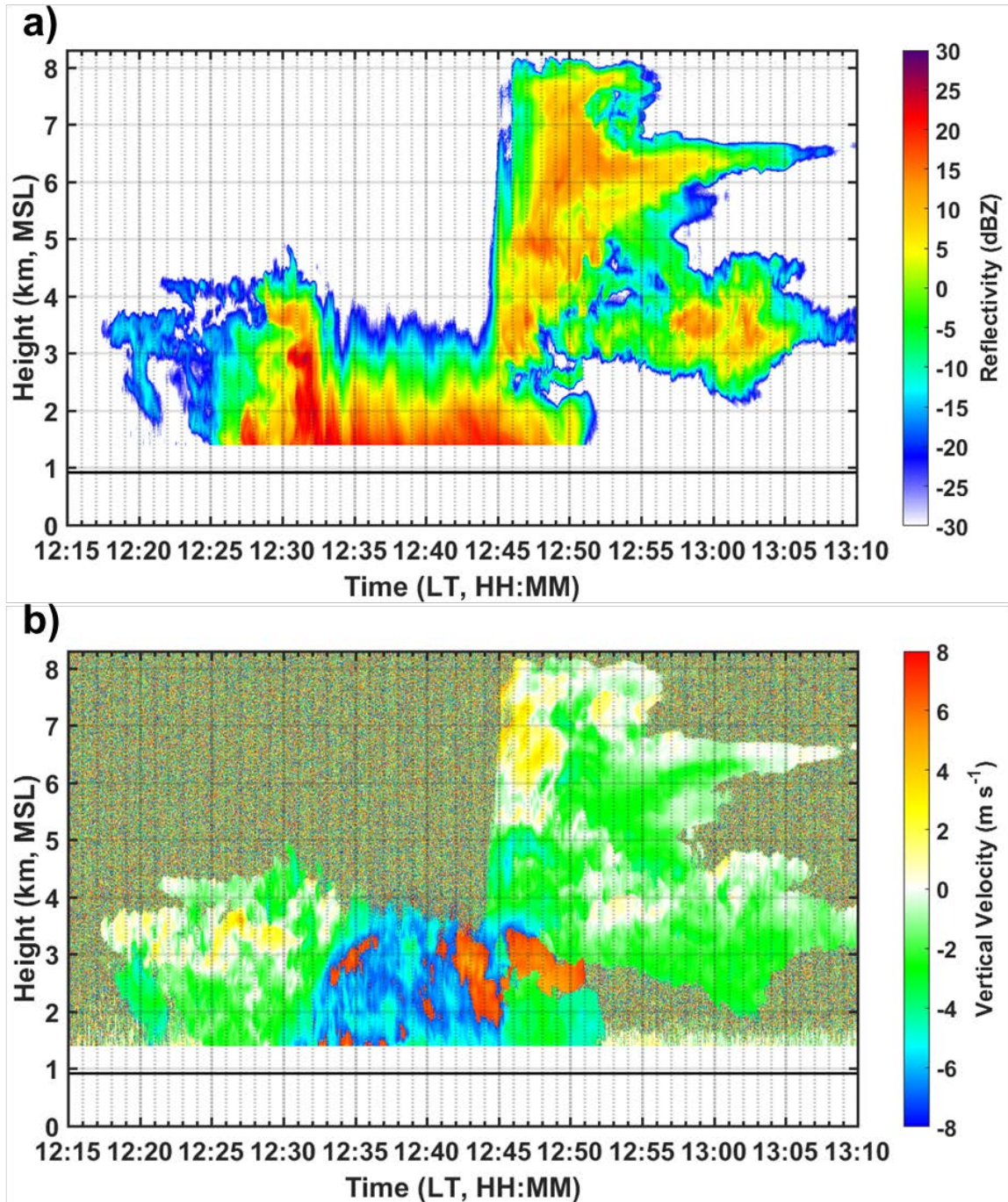


Figure S12: Vertical profiles of W-band reflectivity (a) and vertical velocity (b) of cumulus congestus clouds observed at MV before 12:30 LT on 12 June 2014. The horizontal line depicts the elevation level of the MV supersite (~ 925 m MSL).

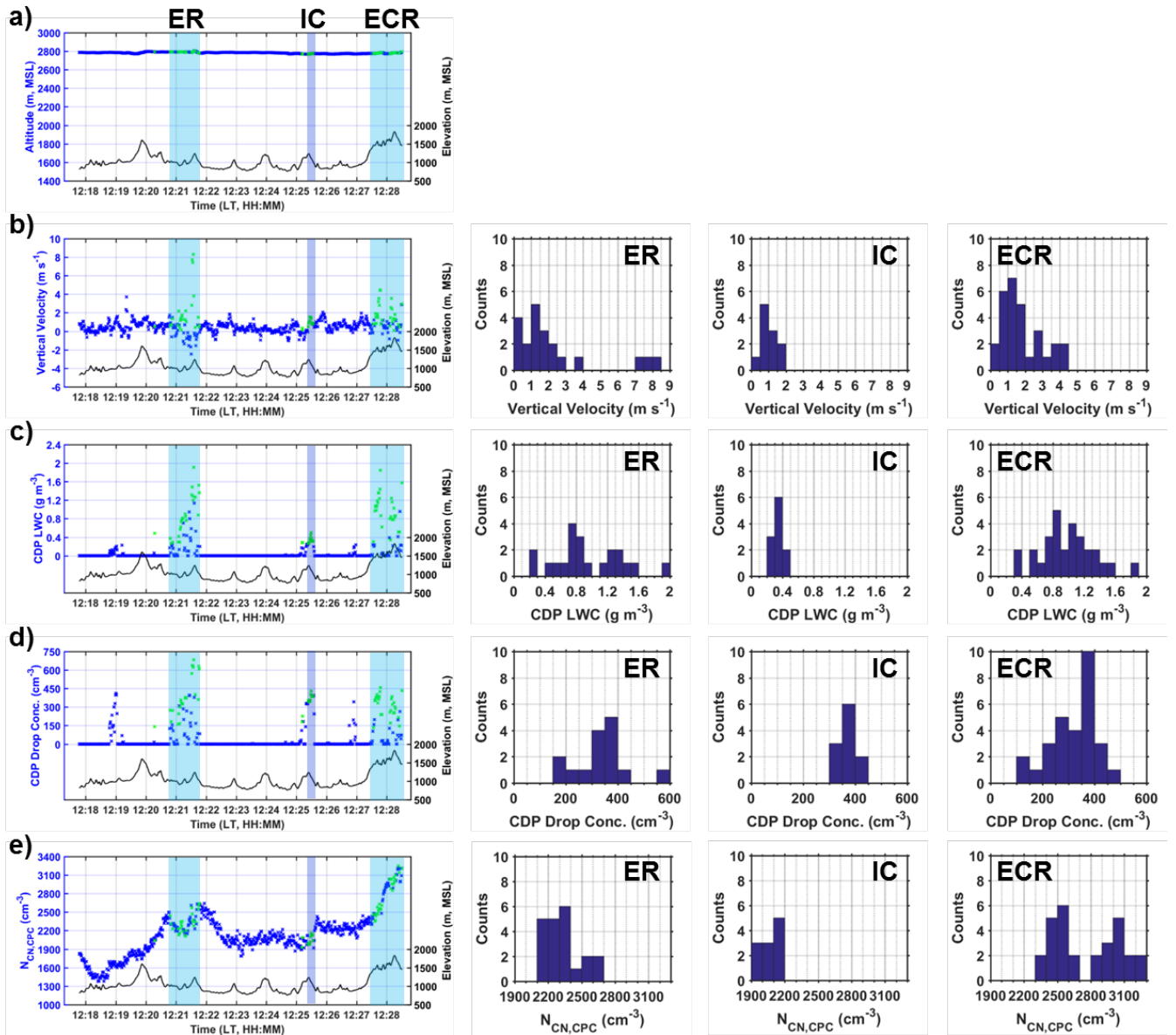


Figure S13: First Column: Time series of flight altitude (a), vertical velocity (b), LWC (c) and drop concentrations (d) from the CDP, and aerosol concentrations from the CPC (e) abroad the UND Citation during the first horizontal leg (see flight track in Fig. 6a). The blue shaded areas correspond to three cloudy regions (from left to right: ER-eastern ridges, IC-targeted in-cloud region, and ECR-Eastern Cherokee reservation), as highlighted in the dark blue circle and light blue boxes in Fig. 3a. Green crosses denote in-cloud samples with a minimum LWC of 0.25 g m^{-3} measured by the CDP. The terrain elevation is represented by the black line. Second to Fourth columns: Histograms of vertical velocity (row b), CDP LWC (row c), CDP drop concentrations (row d), and CPC aerosol concentrations (row e) of in-cloud samples from three cloudy regions, as indicated by green crosses in the first column.

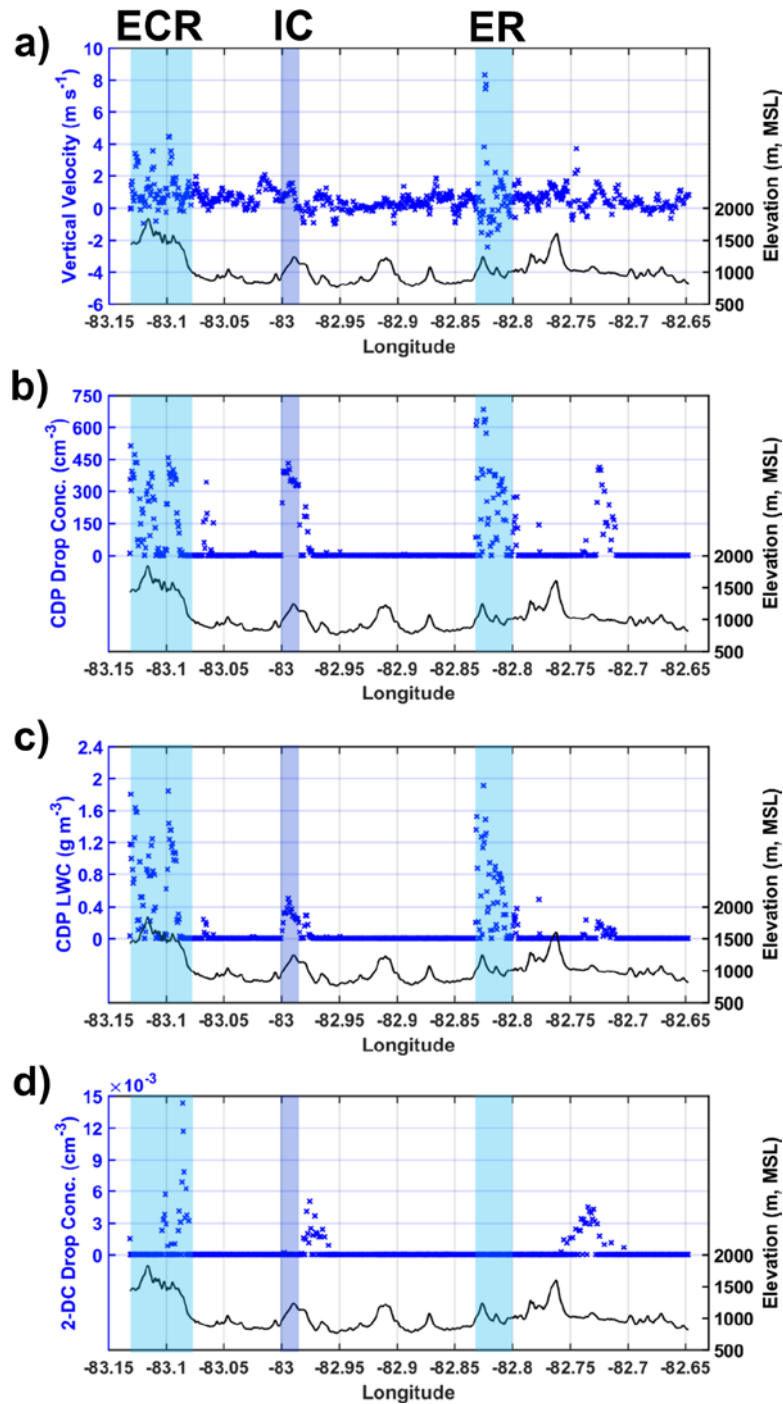


Figure S14: Airborne observations of vertical velocity (a), drop concentrations (b) and LWC (c) from the CDP, and drop concentrations from 2-DC probe (d) aboard the UND Citation during the first horizontal leg (see flight track in Fig. 3a). The blue shaded areas correspond to three cloudy regions (from left to right: ECR-Eastern Cherokee reservation, IC-targeted in-cloud region, and ER-eastern ridges), as highlighted in the dark blue circle and light blue boxes in Fig. 3a. The terrain elevation is represented by the black line.

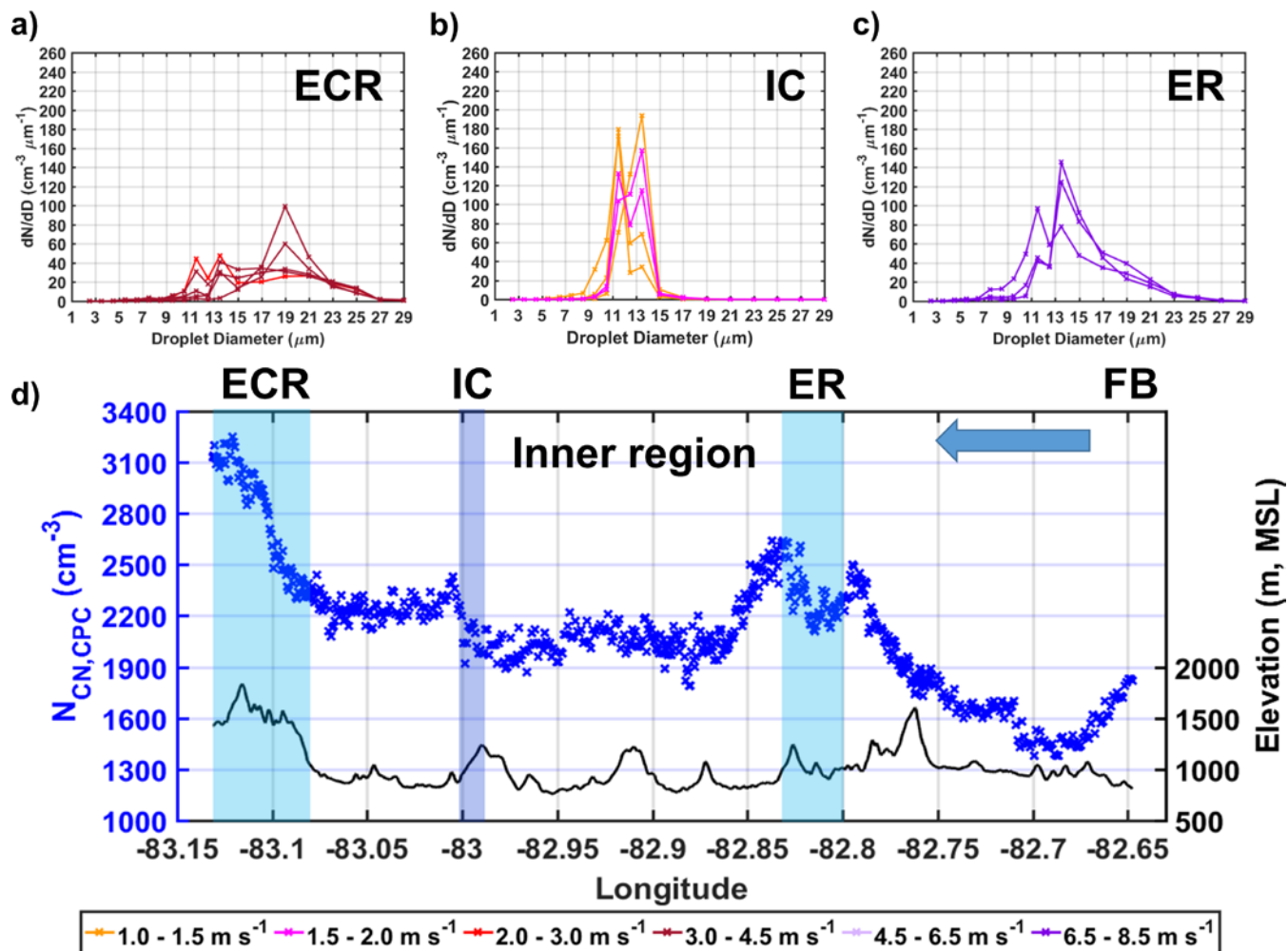


Figure S15: Cloud droplet concentrations at the updraft core of clouds near the Eastern Cherokee reservation (ECR, a), within the targeted in-cloud region (IC, b), and near the foothills of the eastern ridges (ER) over the inner region (c), respectively. Their locations can be referred to Fig. 3a. The updraft velocity of each sample is denoted by its colour. d) Background aerosol concentrations from the CPC abroad the UND Citation during the first horizontal leg (see flight track in Fig. 3a, and the flight direction is indicated by the blue arrow here). Note the airborne aerosol concentrations are not corrected to the standard temperature and pressure (STP). The blue shaded areas correspond to cloudy regions in (a)–(c), also as highlighted in the dark blue circle and light blue boxes in Fig. 3a. The terrain elevation is represented by the black line and FB denotes French Board valley.

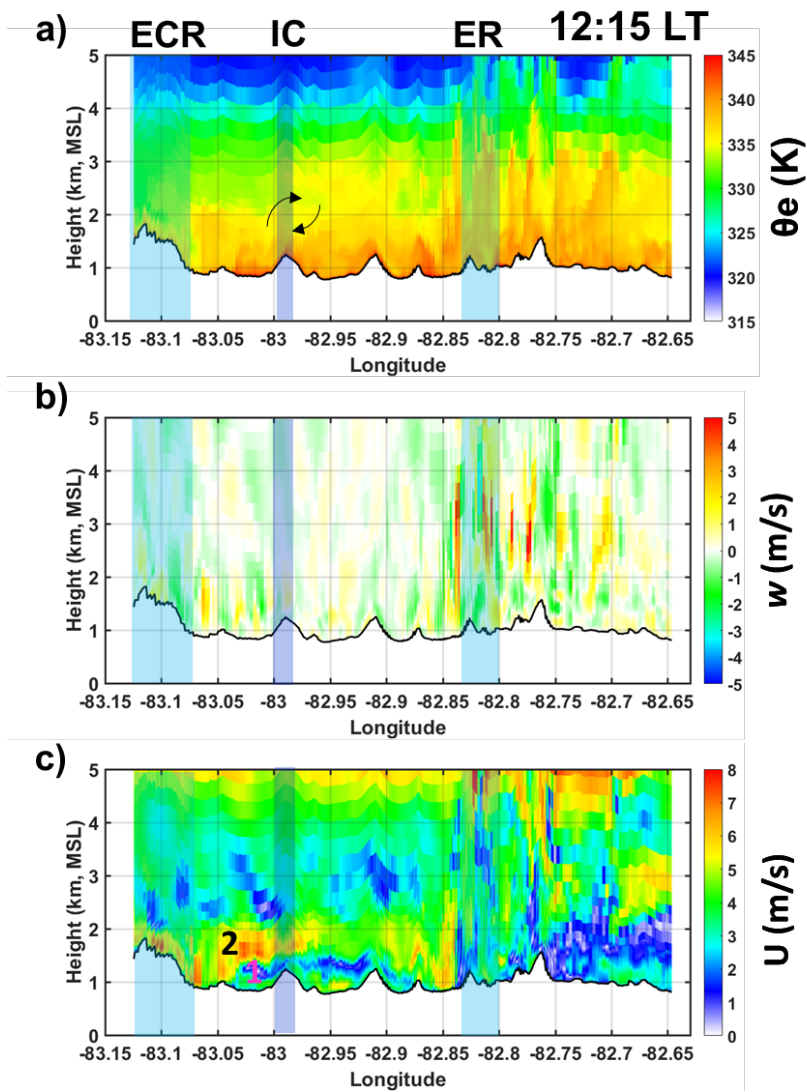


Figure S16: Instantaneous vertical distributions of equivalent potential temperature (θ_e , a), vertical velocity (w , b) and horizontal wind magnitude (U , c) from WRF simulations at 12:15 LT along the trajectory of the first horizontal leg on 12 June 2014. The right-hand panel depicts the strong horizontal wind shear between the valley floor with westerly winds and the southerly winds at ridge level, CBH and above. Note the wind directions at location 1 and 2 at (c) are indicated in the right panel.

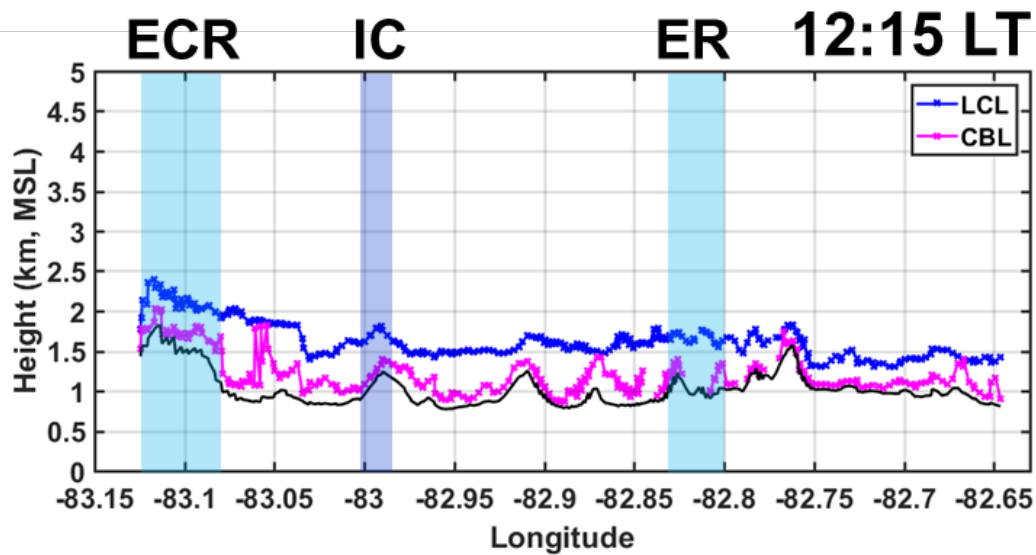


Figure S17: Instantaneous distribution of Lifting Condensation Level (LCL) and Convective Boundary Layer Height (CBL) calculated from WRF simulations at 12:15 LT along the trajectory of the first horizontal leg on 12 June 2014.

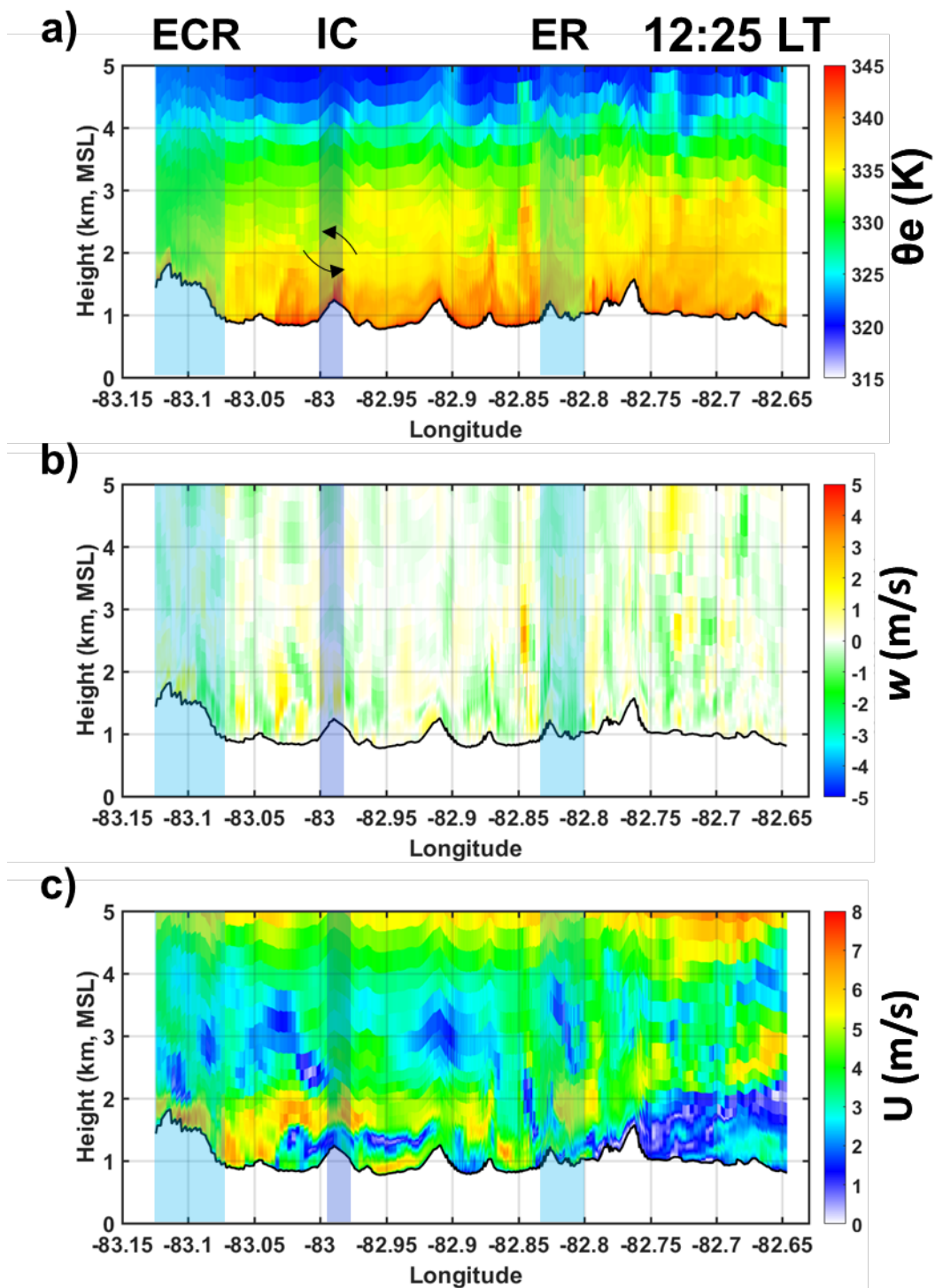


Figure S18: Same as Fig. S16 at a later time (12:25 LT).

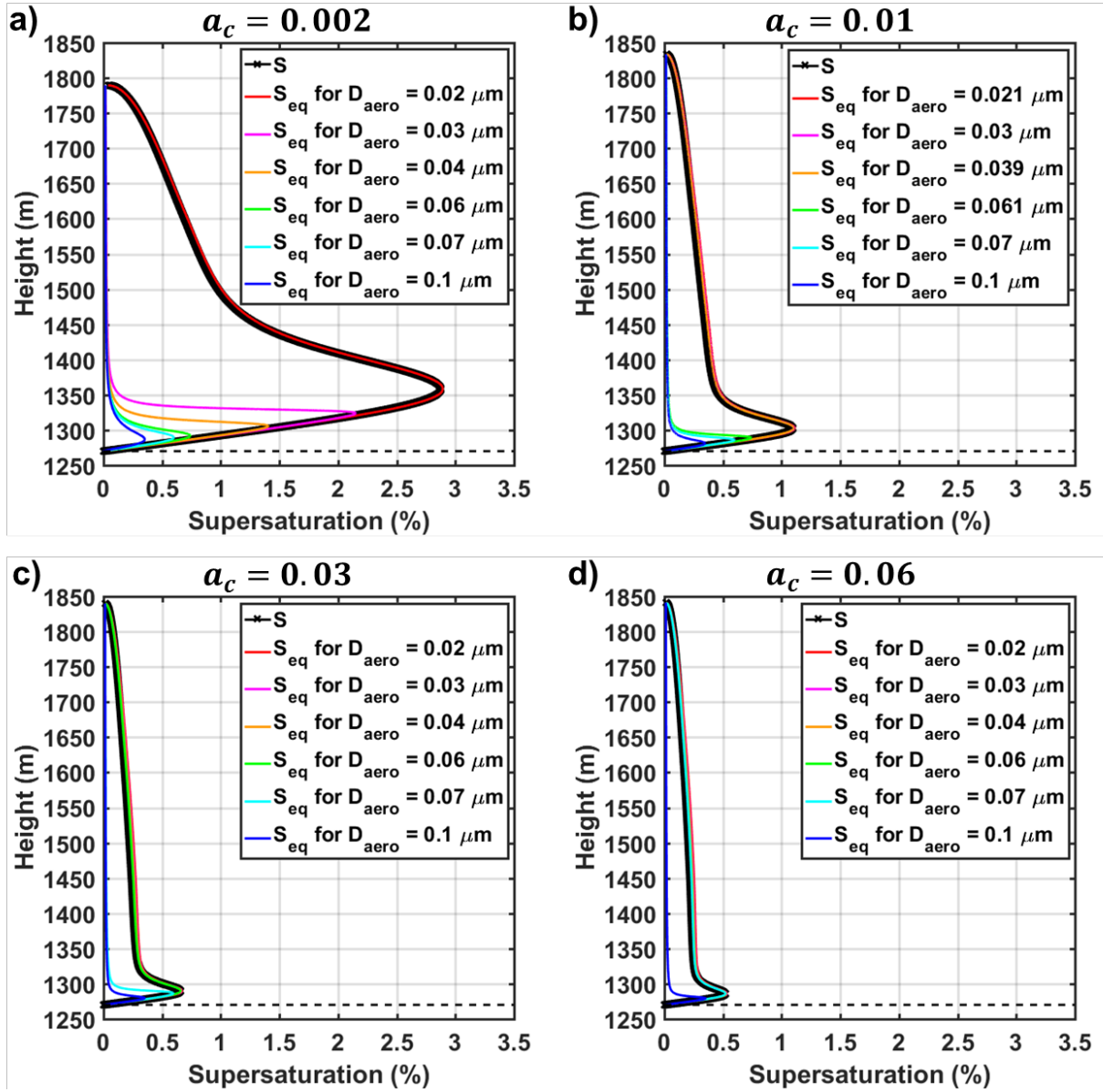


Figure S19: Variations with height of the parcel supersaturation (S , black lines) and droplet equilibrium supersaturation (S_{eq} , coloured lines) for six representative diameters of dry aerosol particles (D_{aero}) for four simulations: a) $a_c = 0.002$, b) $a_c = 0.01$, c) $a_c = 0.03$, and d) $a_c = 0.06$. The horizontal dashed line depicts CBH.

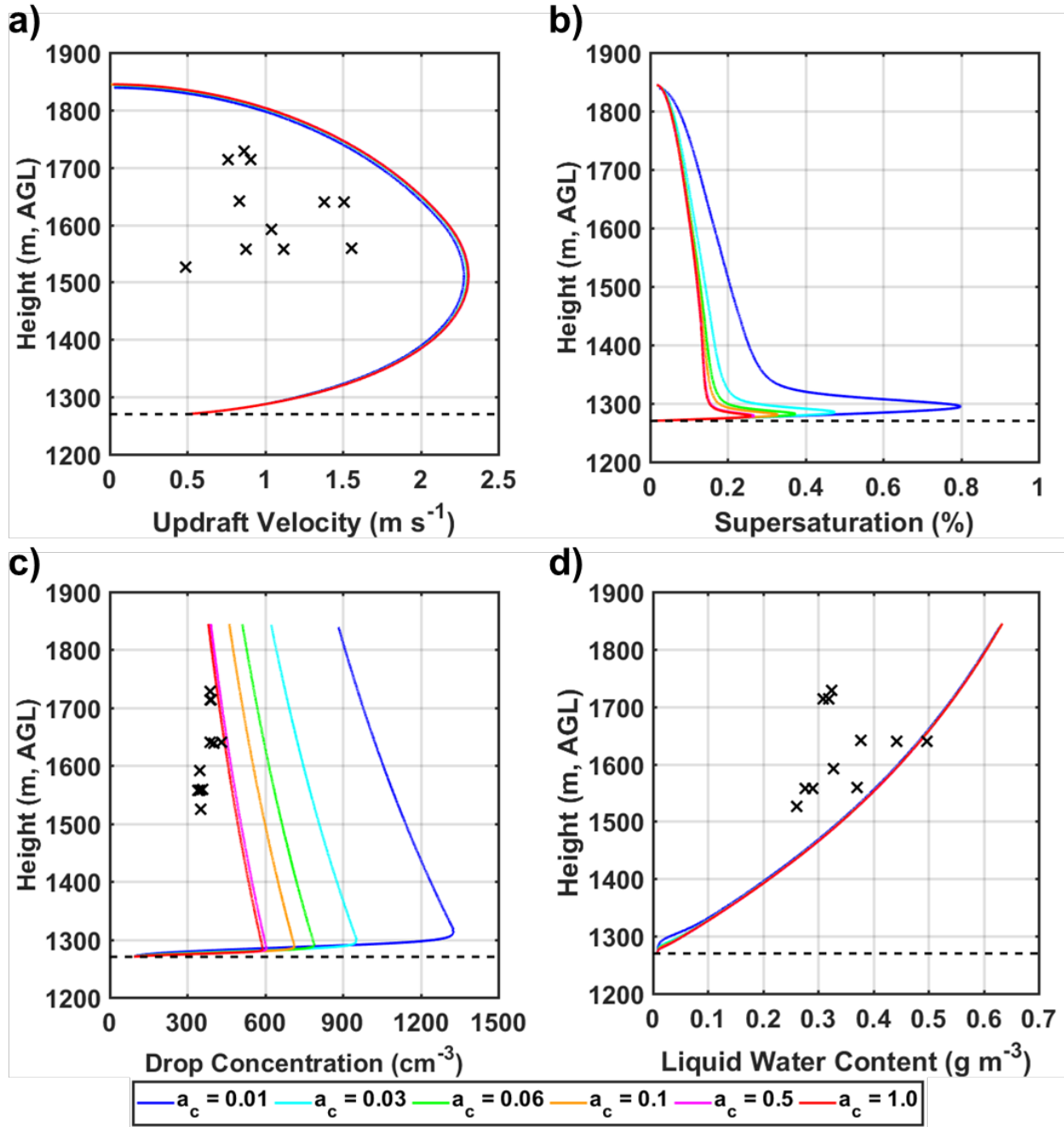


Figure S20: Sensitivity of the updraft velocity (a), supersaturation (b), total drop concentration (c), and LWC (d) to the variations in the condensation coefficient (a_c) as compared to the airborne observations (marked by black crosses). The horizontal dashed line depicts CBH.

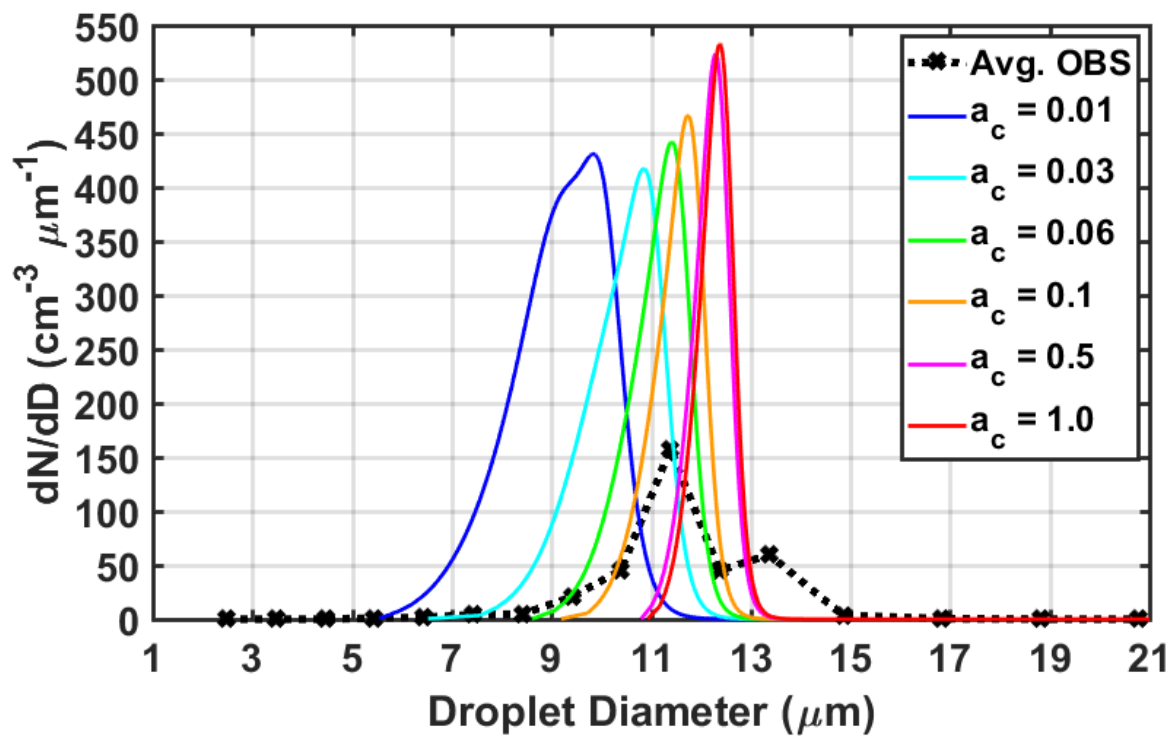


Figure S21: Sensitivity of simulated droplet spectra at 1,600 m (solid lines) to the variations in a_c . The black dotted line reflects the average of five droplet spectra observed by the CDP (dotted lines in Figs. 3c and d) between 1,500 m and 1,600 m AGL.

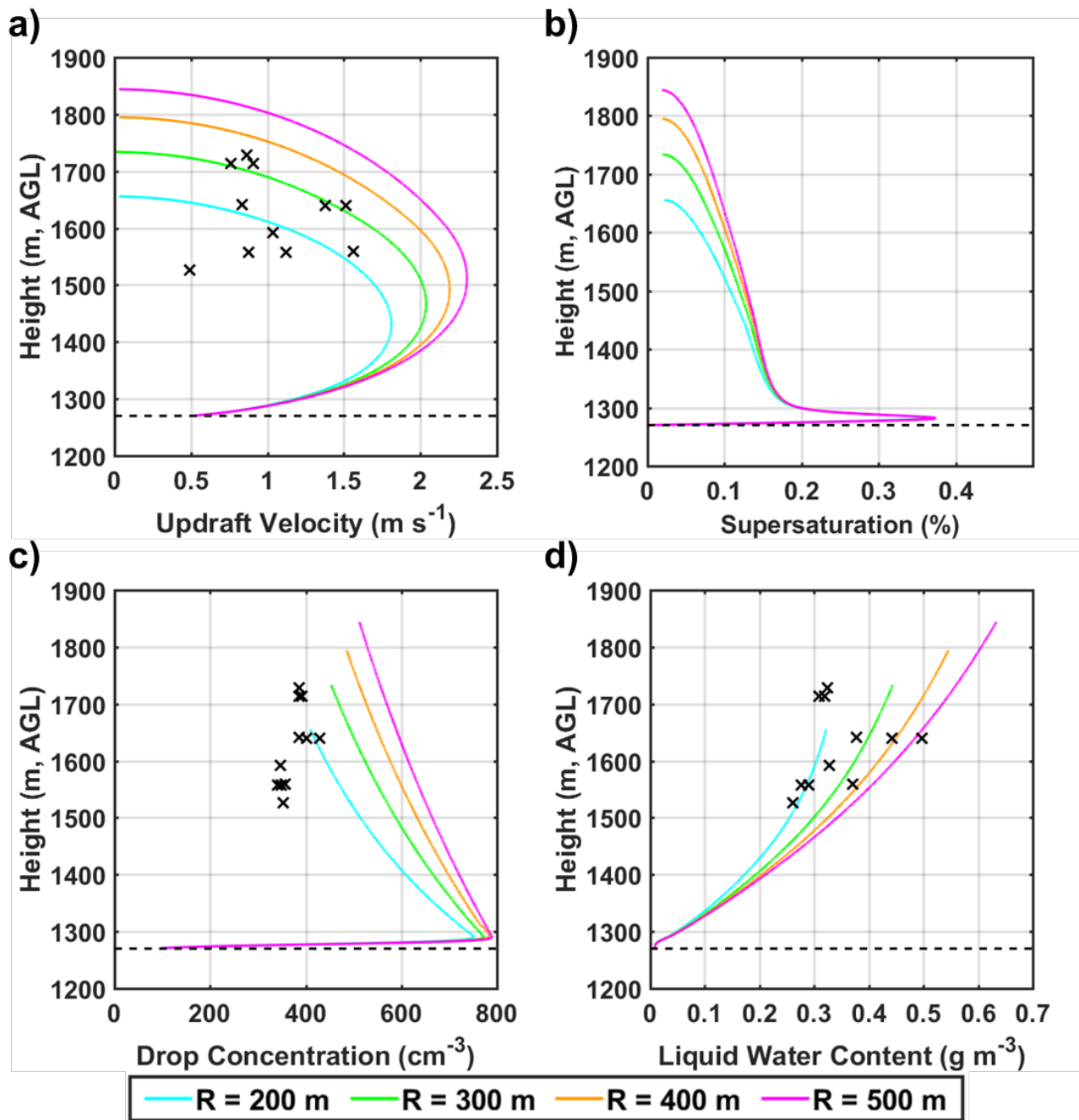


Figure S22: Sensitivity of the updraft velocity (a), supersaturation (b), total drop concentration (c), and LWC (d) to the variations in the initial parcel radius (R) considering lateral entrainment as a bubble model. Note the airborne observations are marked by black crosses, and the horizontal dashed line depicts CBH.

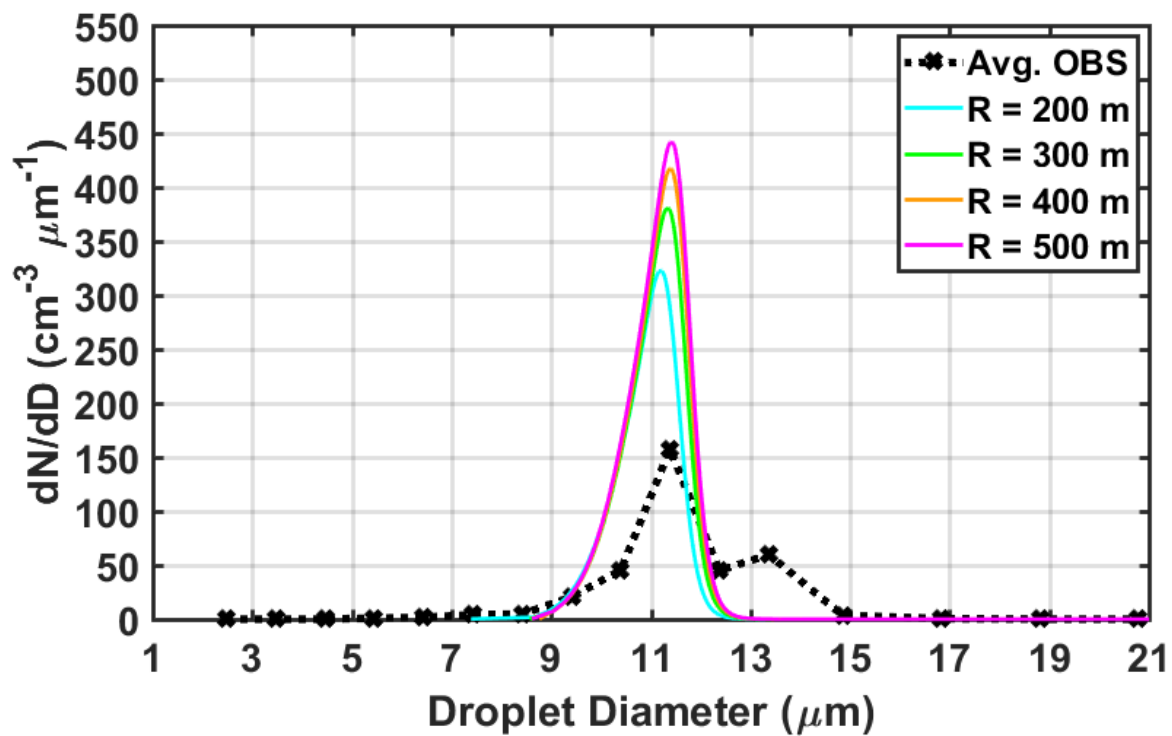


Figure S23: Sensitivity of simulated droplet spectra at 1,600 m (solid lines) to the variations in entrainment strength, represented by the initial parcel radius (R). The black dotted line reflects the average of five droplet spectra observed by the CDP (dotted lines in Figs. 3c and d) between 1,500 m and 1,600 m AGL.